CONF-900821--2

EXPERIMENTAL AND COMPUTATIONAL INVESTIGATION OF THE FUNDAMENTAL MECHANISMS OF CRATERING

by
B. J. Thorne[1], P. J. Hommert[1] and B. Brown[2]

SAND--90-1063C

DE90 009568

ABSTRACT

Early attempts at estimation of stress wave damage in blasting by use of finite element analysis met with limited success due to numerical instabilities that prevented calculations from being carried to late times after significant fragmentation had occurred. A new damage model based on microcrack growth in tension allows finite element calculations which remain stable at late times. Estimation of crater profiles for blasting experiments in granite, using laboratory properties for all parameters, demonstrate a high level of success for this damage model. However, estimated crater profiles show systematic differences from excavated crater profiles which motivate further developments of this model.

INTRODUCTION

In recent years there has been an increasing interest in the development of numerical models for the prediction of rock fragmentation by blasting. These efforts have varied for semi-empirical (Cunningham, 1987; Favreau et al, 1987) to more rigorous (Danell and Leung, 1987; Kuszmaul, 1987a). Numerical modeling of blasting has brought into focus the complexity of the blasting process. Not only are there numerous physical processes occurring, but the host media is geologic and therefore highly variable, with response characteristics that are difficult to quantify and often size dependent. This complexity requires that numerical models be developed in a highly systematic fashion in close coordination with controlled field and laboratory experimentation. It is also important that postulated physical mechanisms undergo thorough numerical evaluation before they can be accepted as being important to the blasting process.

---

1. Sandia National Laboratories
Albuquerque NM 87185-5800 USA
2. Atlas Powder Company
Tamaqua PA 18252 USA

This work performed at Sandia National Laboratories supported by the U. S. Department of Energy under contract DE-AC04-76DP00789.

Since 1985, the Advanced Technology Division at Sandia National Laboratories has been involved in the development of numerical models for describing the blasting process. This work has developed two separate computational thrusts. The initial early time transport of stress is treated through the use of a dynamic wave computer program PRONTO (Taylor and Flanagan, 1987, 1989) and a constitutive damage model that attempts to describe the fracturing that occurs as a result of the stress wave. A separate modeling effort (Preece, 1990) is underway to describe the motion of individual rock fragments as a result of gas flow loading.

This paper describes in detail a model for estimation of stress wave induced fracturing. This model has evolved over a number of years (Kipp and Grady, 1968; Taylor Chen and Kuszmaul, 1986; Kuszmaul 1987a). As will become apparent, modeling stress wave induced fragmentation is very complex and any computational algorithm will only represent an approximation. Thus it is very important that any postulated model be compared in detail against controlled experimental data. Only by such comparisons can it be determined if the numerical embodiment of the physics represents a useful engineering approximation. Traditionally, there has been a lack of highly controlled experimental data. However, in the past two years, as part of our model development program an experimental verification effort has been conducted. The experimental work is being performed jointly with the Atlas Powder Company. Beginning in 1988, two sequences of cratering experiments were conducted for the express purpose of generating data for comparison with model predictions. These experiments examined systematically variations in geometry, rock type, and explosive. Data collected on the tests included continuous detonation velocity, high speed photography of the ground motion, muck pile profiles, excavated crater profiles, and particle size information.

In addition to detailing the numerical model this paper discusses comparisons of the predictions with experimental data. These comparisons have been used to derive our current approach and are being used to identify weaknesses in our current approach which should be targeted in future research. These studies also indicate the complexity of the mechanisms involved and are serving as a basis for developing complimentary numerical descriptions that emphasize different physical processes.

DAMAGE MODEL

The damage model is intended to simulate the dynamic fracture of brittle rock. It is based on work started by Kipp and Grady, 1968 and continued by Taylor, Chen and Kuszmaul, 1986 and Kuszmaul, 1987a. It is modified here to extend it to large crack densities as suggested by Englman and Jaeger, 1987. The essential feature of this model is the treatment of the dynamic fracture process as a continuous accrual of damage in tension, where the damage mechanism is attributed to microcracking in the rock. The fundamental assumption of the model is that the rock is an isotropic material which is permeated by an array of randomly distributed microcracks which grow and interact with one another under tensile loading.

Englman and Jaeger, 1987 introduce a regularized damage parameter, F, which is related to Budiansky and O'Connell's, 1976 crack density, C_d, but takes into account the overlap between the damage volumes of different cracks. To this end they define F by

$$F = 1 - \exp(-\alpha C_d), \qquad (1)$$

where α=16/9. The effective Poison's ratio, ν_e, and bulk modulus, K_e, of a cracked medium with undamaged Poison's ratio ν and bulk modulus K are given by

$$\nu_e = \nu(1 - F) = \nu\exp(-\alpha C_d) \qquad (2)$$

and

$$K_e = (1 - f_1(\nu_e)F)K, \qquad (3)$$

where

$$f_1(\nu_e) = \frac{1 - \nu_e^2}{1 - 2\nu_e}. \qquad (4)$$

In order to relate stress to strain we will generate a system of differential equations which can be solved for the effective elastic moduli of the cracked medium. It is convenient to introduce a damage parameter, D, defined by

$$D = f_1(\nu_e)F. \qquad (5)$$

Note that $0 \le F \le D \le 1$ and

$$K_e = (1 - D)K. \qquad (6)$$

The crack density can be related to an average flaw size, a, by

$$C_d = \gamma N a^3, \qquad (7)$$

where N is the number of active cracks and γ is a proportionality ratio. Differentiating equation 7 yields

$$\frac{dC_d}{dt} = \gamma \frac{dN}{dt} a^3 + 3\gamma N \frac{da}{dt} a^2, \qquad (8)$$

where the forms of N and a are yet to be determined.

At this point, it should be noted that there are a wide variety of assumptions which can be made as to the form of N and there is almost no agreement as to the proper form for flaw size. Kipp and Grady, 1968 and Kuszmaul, 1987a assume that the number of cracks activated at a volumetric strain, ε, is described by a Weibull distribution of the form

$$N = k\varepsilon^m, \qquad (9)$$

where k and m are material dependent constants and the volumetric strain, ε, is one third of the time integral of the trace of the deformation tensor, **d**:

$$\varepsilon = 1/3 \int tr(\mathbf{d}) dt. \qquad (10)$$

Note that ε is positive in tension. Equation 9 implies

$$C_d = k\varepsilon^m a^3 \qquad (11)$$

and

$$\frac{dN}{dt} = mk\varepsilon^{m-1} \frac{d\varepsilon}{dt} \qquad (12)$$

where the proportionality ratio γ has been absorbed in the material constant k. Introducing equations 9 and 12 into equation 8 yields

$$\frac{dC_d}{dt} = mk\varepsilon^{m-1}a^2 \left(a \frac{d\varepsilon}{dt} + \frac{3\varepsilon}{m} \frac{da}{dt} \right). \qquad (13)$$

In the following we will take an approach aimed at modeling the observed dependence of fracture strength and fragment size on strain rate. We will assume that the characteristic flaw size is proportional to the nominal fragment size for dynamic fragmentation of a brittle material. Grady, 1983 derives the following expression for the nominal fragment radius for dynamic fragmentation of a brittle material based on energy considerations at high strain rates:

$$r = \frac{1}{2}\left[\frac{\sqrt{20}K_{IC}}{\rho c R}\right]^{2/3}. \qquad (14)$$

Here K_{IC}, ρ and c are the fracture toughness, density and sound speed of the undamaged material and R is the strain rate, which is assumed in the derivation to be both constant and large.

In order to apply equation 14 to the case where the strain rate is not constant, Taylor, Chen and Kuszmaul, 1986 replace the constant strain rate, R, in equation 14 with the maximum strain rate, R_{max}, which the material has experienced. The derivation of equation 14 assumes that the strain rate R is reached prior to the time of interest, is large and remains constant during the fragmentation process. In the finite element program R_{max} usually occurs when the material first comes off the peak of a shock wave and remains constant after that time. In this case R_{max} is both constant and large, as in the derivation of equation 14. To assure that unreasonably small values of R_{max} are not used in equation 14, a material dependent minimum significant strain rate R_{min} is used until $d\varepsilon/dt$ exceeds R_{min}. Use of equation 14 in this manner results in

$$C_d = \frac{5k\varepsilon^m}{2}\left[\frac{K_{IC}}{\rho c R_{max}}\right]^2 \qquad (15)$$

and da/dt=0. Again the proportionality ratio has been absorbed in the material constant k. Equation 13 becomes

$$\frac{dC_d}{dt} = \frac{5km\varepsilon^{m-1}}{2}\left[\frac{K_{IC}}{\rho c R_{max}}\right]^2 \frac{d\varepsilon}{dt}. \qquad (16)$$

The bulk response of the material is given by $P=K_e\varepsilon$, where the volumetric stress P, which is positive in tension, is one third of the trace of the stress tensor. We assure that the deviatoric response of the material is consistent with the bulk response by defining a degraded shear modulus, μ_e, such that

$$S = 2\mu_e e = \frac{3K_e(1 - 2\nu_e)}{(1 + \nu_e)} e, \qquad (17)$$

where S is the deviatoric part of the stress tensor and e is the deviatoric part of the deformation tensor d. It follows that

$$\frac{dP}{dt} = 3K(1 - D)\frac{d\varepsilon}{dt} - 3K\varepsilon\frac{dD}{dt} \qquad (18)$$

and

$$\frac{dS}{dt} = 2\mu_e \frac{de}{dt} - 2e \frac{d\mu_e}{dt} , \qquad (19)$$

where

$$\frac{d\mu_e}{dt} = \frac{8\nu_e K_e}{(1+\nu_e)^2} \frac{dC_d}{dt} - \frac{3K(1-2\nu_e)}{2(1+\nu_e)} \frac{dD}{dt} . \qquad (20)$$

Equations 2, 4, 5, 16, 18, 19 and 20 constitute a coupled system of algebraic and ordinary differential equations which is solved using a simple centered integration operator in the PRONTO (Taylor and Flanagan, 1987, 1989) finite element programs.

The parameter m relates tensile fracture to strain. The cube root strain rate dependence determined by Grady, 1983 dictates that m=6. This leaves only the parameter k to be defined. Unfortunately, no general definition of k has been found. For the special case of a material with Poisson's ratio zero expanding at a constant strain rate R, it is easy to show that

$$k_0 = \frac{9}{280} \left(\frac{\rho c}{K_{IC}} \right)^2 \left(\frac{18K}{7} \right)^6 \frac{R^2}{P_{max}^6} , \qquad (21)$$

where P_{max} is the maximum volumetric tensile stress achieved in a test to failure at a constant strain rate R. Here we have made use of the fact that m=6 and have written k_0 to emphasize the ν=0 assumption.

Since a rock with a Poisson's ratio of zero would be very strange, a solution of the constant strain rate expansion case without the ν=0 assumption would be more realistic. While it may be possible to solve the constant strain rate expansion case without the ν=0 assumption, we know of no such solution at this writing. However, the same method used to derive equation 21 can be used to solve for $k'(\nu)$, the value of k for a material of constant Poisson's ratio ν. This contradicts equation 2, unless ν=0, but should lend some insight into how k might be expected to depend on ν. The result of this procedure is

$$k'(\nu) = \frac{1-2\nu}{1-\nu^2} k_0 . \qquad (22)$$

Note that $k'(1/2)=0$ and $k'(1/3)=3/8k_0$. This indicates that the ν=0 assumption might result in values of k which are too large.

If laboratory data for maximum tensile stress versus strain rate are not available, it is possible to compute a value for k by using an expression derived by Kipp, Grady and Chen, 1980. For a number of rocks, they found that a reasonable approximation to maximum tensile

stress, P_{max}, as a function of strain rate, R, is given by

$$P_{max} = \left(\frac{9\pi E K_{IC}^2 R}{16 c_s N_s^2} \right)^{1/3} , \qquad (23)$$

where c_s and E are the shear wave velocity and Young's modulus of the undamaged material, and N_s is a shape factor (N_s=1.12 for penny shaped cracks). It is possible to eliminate the ratio R^2/P_{max}^6 between equations 21 and 23 to get

$$k_0 = \frac{29.4 N_s^4}{\pi^2} \left(\frac{K}{K_{IC}} \right)^6 \left(\frac{c_s}{c} \right)^2 . \qquad (24)$$

For ν=0, $(c_s/c)^2$=1/2 and in general

$$\left(\frac{c_s}{c} \right)^2 = \frac{1}{2(1 + \nu)} , \qquad (25)$$

so that use of equation 23 implies that $k'(\nu)$ should be replaced with

$$k''(\nu) = \frac{1 - 2\nu}{(1 - \nu^2)(1 + \nu)} k_0 . \qquad (26)$$

Note that the difference between $k''(\nu)$ and k_0 is greater than the difference between $k'(\nu)$ and k_0, with $k''(1/3)=3/4k'(1/3)=9/32k_0$.

Figure 1 shows the accumulation of damage with strain for uniaxial strain calculations past fragmentation at constant strain rates of 10/s, 100/s and 1000/s. Figure 2 gives volumetric stress as a function of strain for these same three calculations. Note the increase in peak stress with strain rate. The main difference between this version of the model and previous versions is evident at large values of damage, where exponential growth of damage is replaced with an asymptotic approach to the maximum value (D=1). In practice this allows the finite element calculation to remain stable in situations which would have resulted in numerical instability with previous versions.

Thus far we have only considered expansion in tension. Equation 16 implies that damage is healed when the material is recompressed. Since this is not our intent, the damage model is used only when the material is expanding in tension. Previous versions assumed that the material response was governed by the undamaged elastic constants in all other situations. This is equivalent to assuming that the material is identical to the way it was before it was damaged, except when it is expanding in tension. This is illustrated in figure 3, which shows volumetric stress as a function of

strain for a cyclic uniaxial strain calculation in which the material is expanded and recompressed at strain rates of 200/s, 400/s and 600/s. The first cycle stops short of the maximum peak stress and very little damage is accumulated. The second cycle proceeds well past the peak stress and stops just short of fragmentation. The final cycle proceeds well past fragmentation. Note the large amount of dilatancy.

The opposite extreme would be to use the reduced bulk modulus, K_e, and Poisson's ratio, ν_e for recompression in tension, returning to the undamaged moduli only in compression. This is equivalent to assuming that all cracks close exactly and then heal until tension is again applied. This is illustrated in figure 4, which shows volumetric stress as a function of strain for a cyclic uniaxial strain calculation similar to the one illustrated in figure 3. Note the absence of dilatancy.

Since dilatancy is observed in lab tests, it seems reasonable to attempt to build a controlled amount of dilatancy into the model. This can be done by using only a fraction of the damage to compute a partially reduced bulk modulus, K_r, to be used during recompression in tension. A fraction, β, with $0 \le \beta \le 1$, is used to compute the partially reduced bulk modulus according to

$$K_r = (1 - \beta D)K. \qquad (27)$$

The damaged Poisson's ratio is retained in tension and the undamaged elastic moduli are used in compression. When β=1 we have the bulk response illustrated in figure 4. Figure 3 illustrates the bulk response for β=0. Since the reduced Poisson's ratio is always used in tension, the deviatoric response differs from previous versions even for β=0. Figure 5 gives volumetric stress as a function of strain for a cyclic uniaxial strain calculation with β=9/10. On the basis of uniaxial strain calculations, it appears that even values of β near one give significant amounts of dilatancy. In practice, values of β<1/2 have given the best match between calculations and field data.

At high pressures rocks are known to exhibit behavior similar to plasticity in metals. In previous versions this was accounted for by assuming the compressive behavior of the material to be elastic-perfectly plastic. In this version we extend this to account for the increase in yield stress with confining pressure which is observed in triaxial tests. This is done by allowing yield stress to be a function of volumetric stress. In the most

general case, the yield stress in compression is assumed to be an inverse parabola in the absolute value of volumetric stress. This is illustrated in figure 6 using triaxial data for a sandstone. Olsson, 1989 reports two triaxial tests at each of the confining pressures 50, 100 and 200 MPa. All of these tests exhibit clear indications of plastic behavior. If it is assumed that the sample is in a uniform stress state, which it is not, then these data can be plotted as a function of the absolute value of volumetric stress at failure, as in figure 6. The average stresses at the three confining pressures determine an inverse parabola, figure 6, which can be used to determine a yield surface for finite element calculations. If only two confining pressures are used, the function becomes a straight line, and if only one confining pressure is used, elastic-perfectly plastic behavior results. In tension the yield stress is assumed to be very large in order to avoid plasticity.

GRANITE PROPERTIES

Olsson, 1989 reports properties for a granite in which blasting experiments were preformed. Unfortunately, this granite exhibited a foliation which induced anisotropic material properties, violating the most basic assumption on which our model is based. In spite of this, we attempted to model this granite as an isotropic material using the damage model and average properties from tests at 90° and 30° to the foliation. Olsson's data give a density of 2680 kg/m^3. Young's modulus measurements had a large amount of scatter at both angles. After rejecting two suspicious samples, the remaining 16 samples give an average Young's modulus of 62.2 GPa with a standard deviation of 16 GPa. This was confirmed by two zero-stress bar velocity measurements on nonfoliated samples which gave an average Young's modulus of 62.8 GPa. Poison's ratio was obtained for three samples measured at 90° to the foliation. The average of these three values was 0.29 with a standard deviation of 0.05.

Kolsky bar tests were used to determine the minimum strain rate at which to apply equation 20. Figure 7 shows failure stress as a function of strain rate at 90° to the foliation for three uniaxial tests and four Kolsky bar tests at strain rates between 100/s and 200/s. A cube root dependence of failure strength on strain rate drawn through the average of the four Kolsky bar tests results in the steeply sloping line on the right. This

line drops below the average of the three uniaxial tests at a strain rate of 9.8/s. Assuming that the cube root dependence of failure stress on strain rate applies down to a strain rate of 20/s results in the piecewise liner fit shown in figure 7. The slope of the left hand segment is somewhat arbitrary, but seems reasonable.

Unfortunately none of the triaxial tests exhibited indications of plasticity. We decided to treat the uniaxial and triaxial failure strengths as lower bounds on the plastic limit and construct an inverse parabolic yield surface well above these data. Figure 8 shows failure strengths for 8 uniaxial tests, 9 triaxial tests at a confining pressure of 50 MPa and two triaxial tests at a confining pressure of 200 Mpa (Olsson, 1989 inadvertently omitted the two tests at 200 MPa). All of these data are plotted as a function of the absolute value of the stress which would result from assuming that the samples were in a uniform stress state at the time of failure. Note the large amount of scatter. The lower curve in figure 8 is the inverse parabola determined by the average failure stress at each confining pressure. The upper curve in figure 8 is the inverse parabola used as a yield surface in the damage model.

Chong et al, 1988 measured K_{IC} values for this granite at angles of 0°, 45° and 90° to the foliation. These measurements confirmed the anisotropic nature of the site. Ignoring the anisotropy and using divider geometry, an average value of 1.67 MPa$\sqrt{m}$ with a standard deviation of 0.41 MPa$\sqrt{m}$ was obtained for K_{IC}. In the total absence of any data on maximum tensile stress as a function of strain rate, we calculated $k=8.2\times10^{24}/m^3$ from equation 26.

CALCULATIONS

In an attempt to model blasting experiments in granite, two-dimensional axisymmetric finite element calculations were preformed using the damage model and the PRONTO 2D finite element program. The isotropic material properties discussed above were used without any adjustments being made to improve agreement between the calculations and the experiments. It was necessary to use one of the experiments as a basis for choosing the value of β to be used for recompression in tension. This will be discussed below.

Three depths of burial were simulated. Part of the finite element configuration for simulation of the three meter depth-of-burial blasting experiments is shown in figure 9. An

axis of rotational symmetry is assumed along the center the borehole. The 5 3/4" diameter of the borehole dictates that the center column of elements have radial dimension 0.073025 m. The radial dimension of the elements increases with radius, requiring 67 elements between the axis of rotational symmetry and a nonreflecting boundary at a radius of 15 meters. A vertical dimension of 1/8 of a meter is used between the bottom of the borehole at a depth of 3.5 meters and the free boundary at the surface. The vertical dimension of the elements below the borehole is increased with depth. There are 63 elements between the surface and nonreflecting boundary at a depth of 20 meters, for a total of 4,221 elements. The explosive charge is modeled by the eight elements blacked out in figure 9 along the axis of rotational symmetry between the 2.5 and 3.5 meter depths. The finite element configurations for simulation of the two and four meter depth-of-burial blasting experiments are generated from the three meter depth-of-burial configuration by moving the depth of the explosive charge and the bottom boundary up by one meter in the two meter depth-of-burial case, resulting in 3,886 elements and down by one meter in the four meter depth-of-burial case, resulting in 4,757 elements.

Except for the eight elements representing the explosive charge, all elements are assumed to represent solid granite and are modeled using the above material properties in the damage model. This includes elements in the borehole above the charge. In the blast experiments, the borehole is filled with a loose packed stemming material which would be impossible to model in the finite element calculations. Assuming that the borehole above the charge is solid granite, rather than a loose packed stemming material, would invalidate gas flow and particle motion calculations, but should have little effect in the short time frame of these finite element stress wave calculations.

The explosive charge is modeled using the JWL (Dobratz, 1981) equation-of-state. Atlas Powder APEX 1220 and ANFO charges were simulated at each depth-of-burial. The APEX 1220 was modeled as having 1250 kg/m^3 density, 6065 m/s detonation velocity and 2.6×10^9 J/m^3 energy density. The ANFO was modeled as having 830 kg/m^3 density, 3780 m/s detonation velocity and 7.08×10^9 J/m^3 energy density.

CALCULATED CRATER PROFILES

Kuszmaul, 1987b applies three-dimensional percolation theory to derive a fragmentation criterion based on crack densities calculated with his fragmentation model. The only modification of this theory necessary for use with the current damage model is that the fragmentation limit must be based on the regularized damage parameter rather than the crack density. This leads to a fragmentation limit of F=0.693.

Figure 10 shows the fragmented region limit as predicted by the calculated 0.693 contour for a one meter APEX 1220 charge centered at a three meter depth. Only the right half of the calculated fragmentation limit is shown since the left half would be a mirror image of the right half. The position of the explosive charge is indicated by the slant shaded region at the bottom of the borehole. This is compared to perpendicular profiles of the excavated crater from a blasting experiment. The differences between the two profiles of the excavated crater are probably caused by foliation at the test site, and is large enough to indicate that foliation has a significant effect on the cratering process. A second blast experiment at this same depth gave similar crater profiles. With the exception of an almost isolated region near the top of the charge, the calculated edge of the fragmented region falls between the two excavated crater profiles. Notice that the calculation predicts an unbroken region at the surface above the edge of the fragmented region. In the blasting experiments the edge of the crater was ringed with large undamaged pieces of approximately the predicted thickness. The circles near the bottom of the borehole mark elements which did not go into tension during the calculation, probably as a result of plasticity.

In this calculation a value of β=0 was used for recompression in tension. Equally good agreement was obtained with several values of $\beta \leq 1/2$. Values of β greater than 1/2 lead to damage adjacent to the borehole, which was not observed in either of the three meter depth-of-burial experiments. We chose a value of β=0 based on agreement with this experiment and the fact that previous versions of the model have all used this amount of dilatancy. We did not allow any further adjustment of material properties to improve agreement with other blasting experiments.

Figure 11 compares the fragmented region limit as predicted by the calculated 0.693

contour, with profiles of the excavated crater from a blasting experiment using a one meter APEX 1220 charge centered at a two meter depth. Again, a second blast experiment at this same depth gave similar crater profiles. The two perpendicular profiles of the excavated crater do not intersect at the center of the crater due to surveying errors. The radius of the calculated fragmented region agrees with the excavated crater radius quite well. However, the excavated crater extends to the bottom of the charge, while the calculated fragmented region only extends to the top of the charge. In fact the calculation predicted very little damage near the charge, with five elements near the bottom of the charge remaining in compression during the entire calculation. This region experiences a significant amount of plastic strain which limits tensile stresses. Since no plasticity data was available for this material, the way plasticity was treated is one of the most questionable aspects of the model and could be the cause of the shallow depth of the calculated fragmented region. However, it may be that the break up of the material adjacent to the charge is a result of gas flowing into radial cracks and breaking it up as it is lifted from the crater. Obviously such mechanisms cannot be predicted by any method that considers only shock wave effects.

Figure 12 compares the fragmented region limit as predicted by the calculated 0.693 contour, with a profile of the excavated crater from a blasting experiment using a one meter APEX 1220 charge centered at a four meter depth. Only one profile of the excavated crater is shown because of surveying errors in the perpendicular profile. However, a shift in the data for the perpendicular profile gave a similar crater profile as did a second blast experiment at this same depth. The radius of the calculated fragmented region agrees reasonably well with the excavated crater radius. However, the excavated crater extends to a depth of 1.8 m, while the calculated fragmented region only extends to a depth of about 0.6 m. The excavated crater was quite symmetric so it is difficult to argue that the disagreement is caused by the anisotropy of the site. Note that the calculation predicts two large fragmented regions below the excavated crater. This damage occurs before the shock wave reaches the surface and could remove a significant amount of energy from the shock wave. If the calculations are over predicting damage during this early time, then the energy removed from the shock wave before it reached the surface would explain why this calculation

under predicts crater depth. However, this same argument would lead us to attribute the good agreement between the calculated fragmented region and the excavated crater profiles in figure 10 to a fortuitous combination of too much damage at early time and too little at late time.

Large differences between the excavated crater profiles for the two blasting experiments using ANFO at the three meter depth-of-burial complicate efforts to compare them with calculations. Figure 13 compares the limit of the fragmented region as predicted by the calculated 0.693 contour, with profiles of the excavated crater from one of the blasting experiments using a one meter ANFO charge centered at a three meter depth. The excavated crater is approximately the same size as obtained with APEX 1220, but the calculation predicts a very small fragmented region. In this case, comparison with the experimental results are not appropriate due to a basalt dike which cuts through the excavated crater but could not be modeled in the calculation. A second blast experiment away from the basalt dike at the same depth gave a much smaller excavated crater, in fairly good agreement with the calculated fragmented region as shown in figure 14. However, this blast experiment may also be inappropriate for comparison with the calculation due to a measured detonation velocity of only 2/3 of the detonation velocity used for ANFO in the calculation.

At the two meter depth-of-burial, figure 15, agreement between the fragmented region predicted by the calculation and an excavated crater profile is similar to the results with APEX 1220 at the same depth-of-burial. At the four meter depth-of-burial, figure 16, the agreement between the calculated fragmented region and the excavated crater is almost exact. Each of these blast experiments was confirmed by a second blast experiment. Note that none of the ANFO calculations predicted large fragmented regions below the crater. This might indicate that the damage calculated at early time is related to loading rate since the most dramatic difference between APEX 1220 and ANFO, at least as modeled in the calculations, is the detonation velocity.

CONCLUSIONS

The current damage model is a significant improvement over previous versions mainly because it allows calculations even when a large amount of damage is predicted. This allows simulation times large enough to be sure

that no shock wave induced damage can occur at later times. These calculations can be carried out in as little as one percent of the computer time required for calculations with previous versions, even though it was necessary to terminate calculations at shorter simulation times with previous versions. The increased speed is important because it allows efficient parameter variation to evaluate the effects of variation in and uncertainties about material properties and will allow very large three-dimensional finite element models to be used at a reasonable cost.

Comparison of calculations with blast experiments in granite indicate that reasonable results can be obtained with the current damage model even using average material properties for an anisotropic site. However, significant discrepancies between the calculated fragmented regions and the excavated craters are evident. Comparison with experiments in a wide variety of isotropic rocks must be carried out before it will be known whether or not the current version of the model is a useful engineering tool. Certainly the current version of the model is not theoretically perfect, and further tests are likely to indicate areas where the current version of the model can be improved.

In the derivation of the model we have tried to indicate where future efforts are likely to yield improvements. A more realistic interpretation of the parameter k, introduced in equation 9 and a means of calculating it from lab tests seems essential. Of course, the proper solution to this might be the use of another form for the number of cracks opened. The use of equation 14 in determining the characteristic flaw size has the advantage of introducing standard material parameters into the model, but requires the acceptance of a characteristic flaw size that depends on a previously determined maximum strain rate and does not grow with the application of tensile stress. While plasticity is a well established theory for metals, the assumption that a rock can flow plasticity without accumulating damage is at best questionable. Perhaps the theory can be modified to include a link between plastic strain and damage accumulation in compression. Certainly a more realistic treatment of dilatancy is needed.

Beyond these details, it might be necessary to examine some of the more basic assumptions of the model. For an anisotropic material the assumption that microcracks are randomly distributed and oriented is probably not valid. Of course, introduction of anisotropy would require that all calculations

be three-dimensional and that a new anisotropic finite element program be developed. It seems that the activation of damage could depend on the full stress tensor and not be limited to situations which result in volumetric tension. Budiansky and O'Connell's equivalent elastic moduli and Englman and Jaeger's extension to large crack densities are only intended to be approximations. It may be possible to replace these with more accurate approximations. Given the complexities of this approach we intend to explore other computational approaches as well as evolutionary modifications to the current model.

REFERENCES

Budiansky, B. and O'Connell, R. J., 1976. "Elastic Moduli of a Cracked Solid," Computer Methods in Applied Mechanics and Engineering," vol. 12, pp. 81-97.

Chong, K. P., Basham, K. D., Wang, D. Q. and Estes, R. J., 1988. "Fracture Toughness Characterization of Eastern Basalt and Gneiss," KPC & Associates report to Sandia National Laboratories on contract No. 55-5698, Laramie, WY.

Cunningham, C. V. B., 1987. Fragmentation Estimations and the KUZ-RAM Model - Four Years On," in Proceedings of the Second International Symposium on Fragmentation by Blasting, (Keystone, CO).

Danell, R. E. and Leung, L., 1987. "Computer Simulation of Blast Fracture and Fragmentation of Rocks," in Proceedings of the Second International Symposium on Fragmentation by Blasting, (Keystone, CO).

Dobratz, B. M., 1981. "LLNL Explosives Handbook - Properties of Chemical Explosives and Explosive Stimulants," DE85-015961 Lawrence Livermore National Laboratory, Livermore, CA.

Englman, R. and Jaeger, Z., 1987. Theoretical Aids for Improvement of Blasting Efficiencies in Oil Shale and Rocks," Soreq Nuclear Research Center, Israel.

Favreau, R. F., Kuzyk, G. W., Babulic, P. J., Morin, R. A. and Tienkamp, N. J., 1987. "The Use of Computer Blast Simulations to Improve Blast Quality," in Proceedings of the Second International Symposium on Fragmentation by Blasting, (Keystone, CO).

Grady, D., 1983. "The Mechanics of Fracture Under High-Rate Stress Loading," in William Prager Symposium on Mechanics of Geomaterials: Rocks, Concretes and Soils, (Bazant, Z. P., ed).

Kipp, M. E. and Grady, D. E., 1968.
"Numerical Studies of Rock Fragmentation," SAND79-1582, Sandia National Laboratories, Albuquerque, NM.

Kipp, M. E., Grady, D. E. and Chen, E., 1980.
"Strain-Rate Dependent Fracture Initiation," International Journal Of Fracture, vol 16.

Kuszmaul, J. S., 1987a.
"A New Constitutive Model for Fragmentation of Rock Under Dynamic Loading," in Proceedings of the Second International Symposium on Fragmentation by Blasting, (Keystone, CO), pp 412-423.

Kuszmaul, J. S., 1987b.
"A Technique for Predicting Fragmentation and Fragment Sizes Resulting from Rock Blasting," in Proceedings of the 28th U. S. Symposium on Rock Mechanics, Tucson, AZ.

Olsson, W. A., 1989.
"Quasi-Static and Dynamic Mechanical Properties of a Granite and a Sandstone," SAND89-1197, Sandia National Laboratories, Albuquerque, NM.

Preece, D. S. and Taylor, L. M., 1990.
"Spherical Element Bulking Mechanisms for Modelling Blast Induced Rock Motion," Third International Symposium on Rock Fragmentation by Blasting, Brisbane, Queensland, Australia.

Taylor, L. M., Chen, E. and Kuszmaul, J., 1986.
"Microcrack-Induced Damage Accumulation in Brittle Rock Under Dynamic Loading," Computer Methods in Applied Mechanics and Engineering, vol. 55, no.3, pp. 301-320.

Taylor, L. M. and Flanagan, D. P., 1987.
"PRONTO 2D A Two-Dimensional Transient Solid Dynamics Program," SAND86-0594, Sandia National Laboratories, Albuquerque, NM.

Taylor, L. M. and Flanagan, D. P., 1989.
"PRONTO 3D A Three-Dimensional Transient Solid Dynamics Program," SAND87-1912, Sandia National Laboratories, Albuquerque, NM.

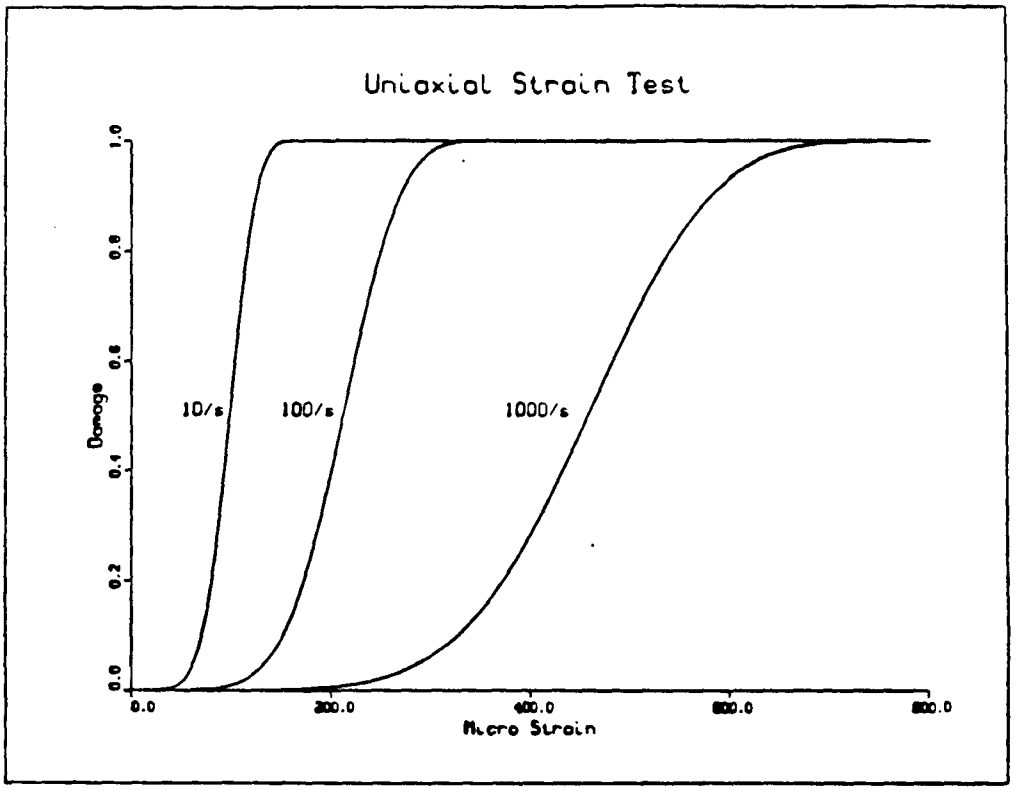

FIGURE 1 Damage as a function of strain for uniaxial strain calculations at strain rates of 10/s, 100/s and 1000/s

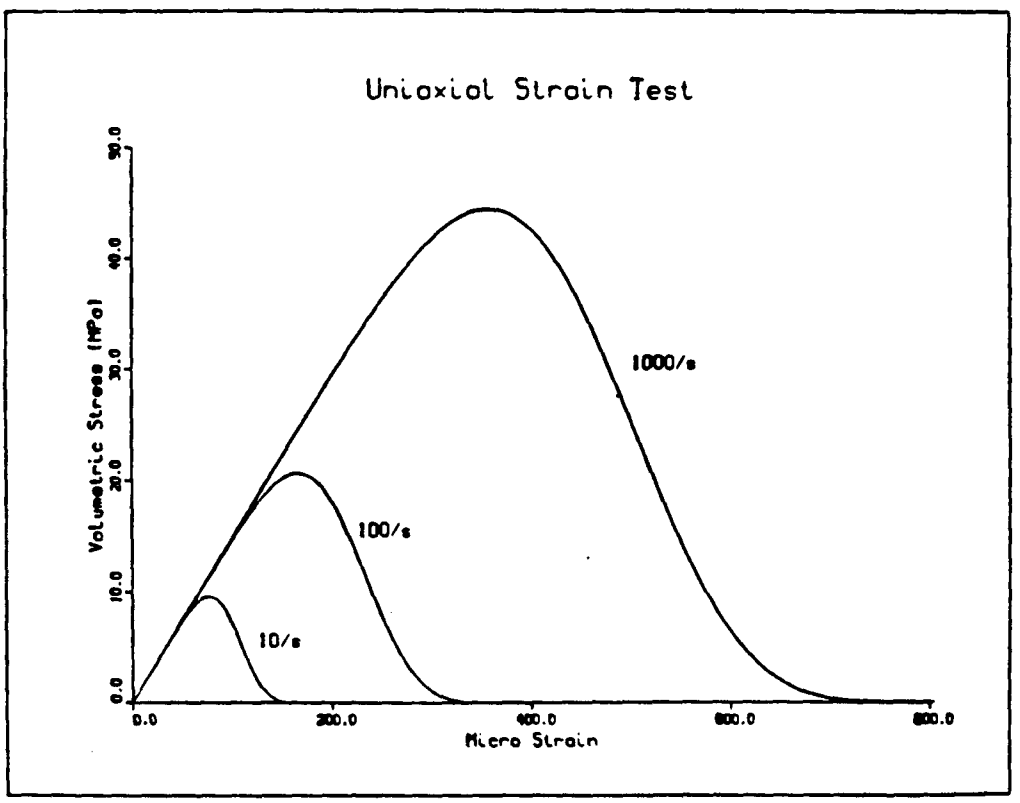

FIGURE 2 Volumetric stress as a function of strain for uniaxial strain calculations at strain rates of 10/s, 100/s and 1000/s

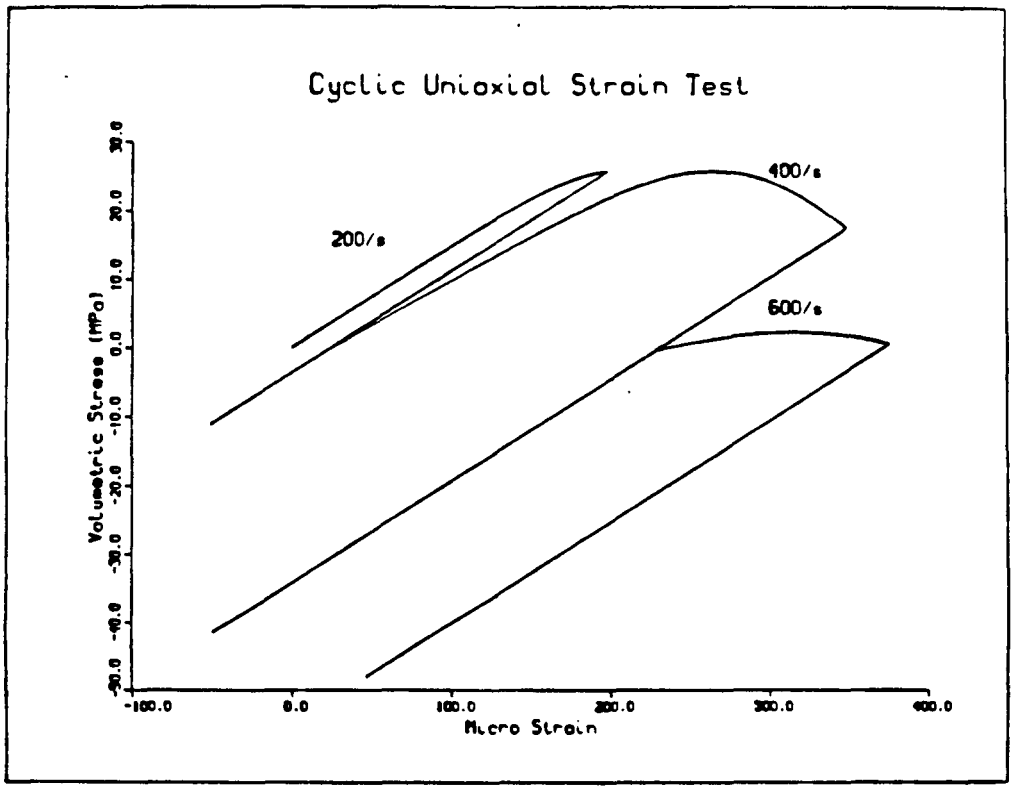

FIGURE 3 Volumetric stress as a function of strain for a cyclic uniaxial strain calculation at strain rates of 200/s, 400/s and 600/s, with undamaged properties used for recompression (β=0)

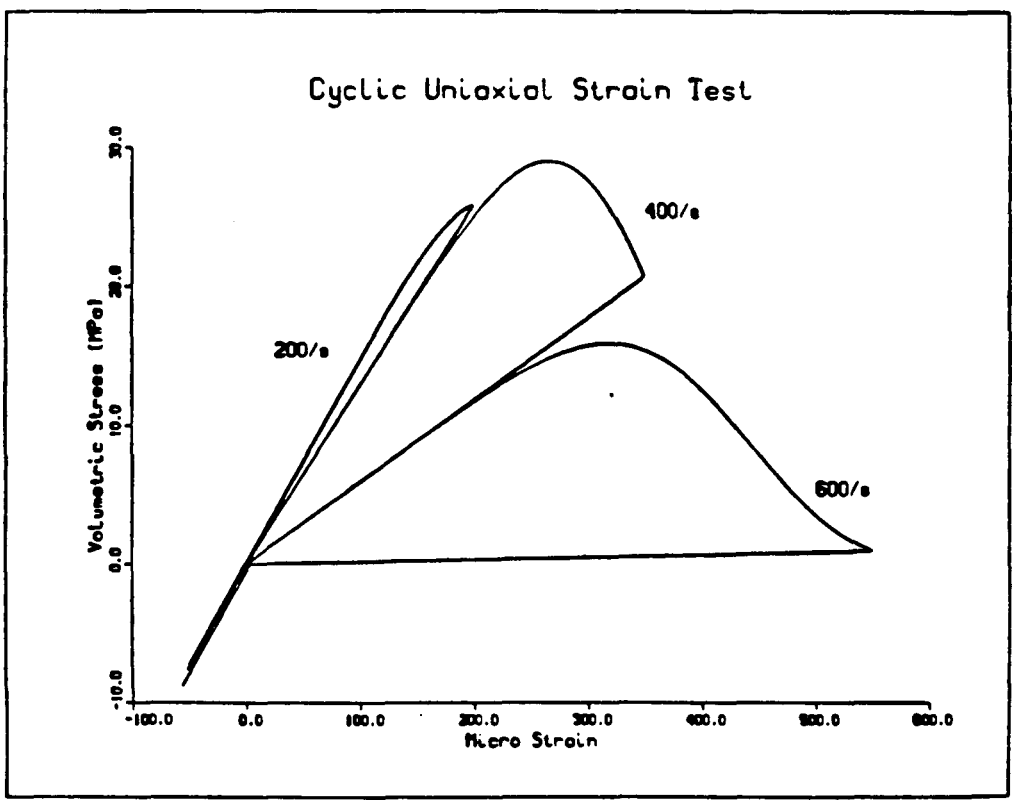

FIGURE 4 Volumetric stress as a function of strain for a cyclic uniaxial strain calculation at strain rates of 200/s, 400/s and 600/s, with damaged properties used for recompression (β=1)

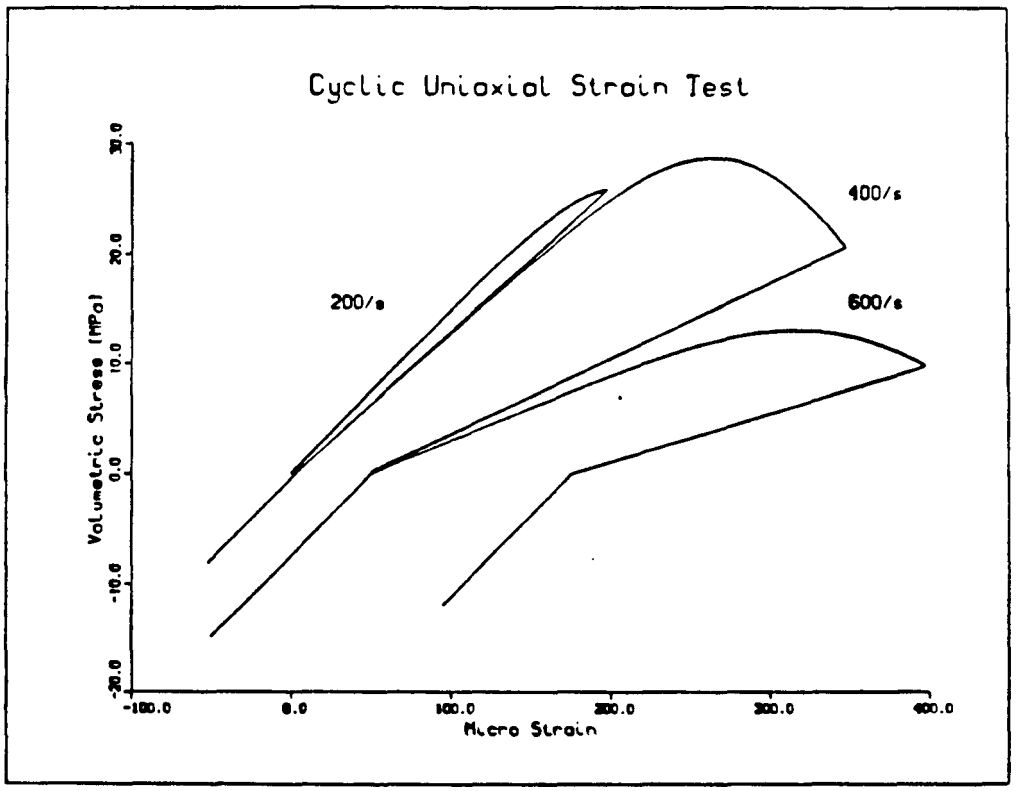

FIGURE 5 Volumetric stress as a function of strain for a cyclic uniaxial strain calculation at strain rates of 200/s, 400/s and 600/s, with K_r computed using β=9/10

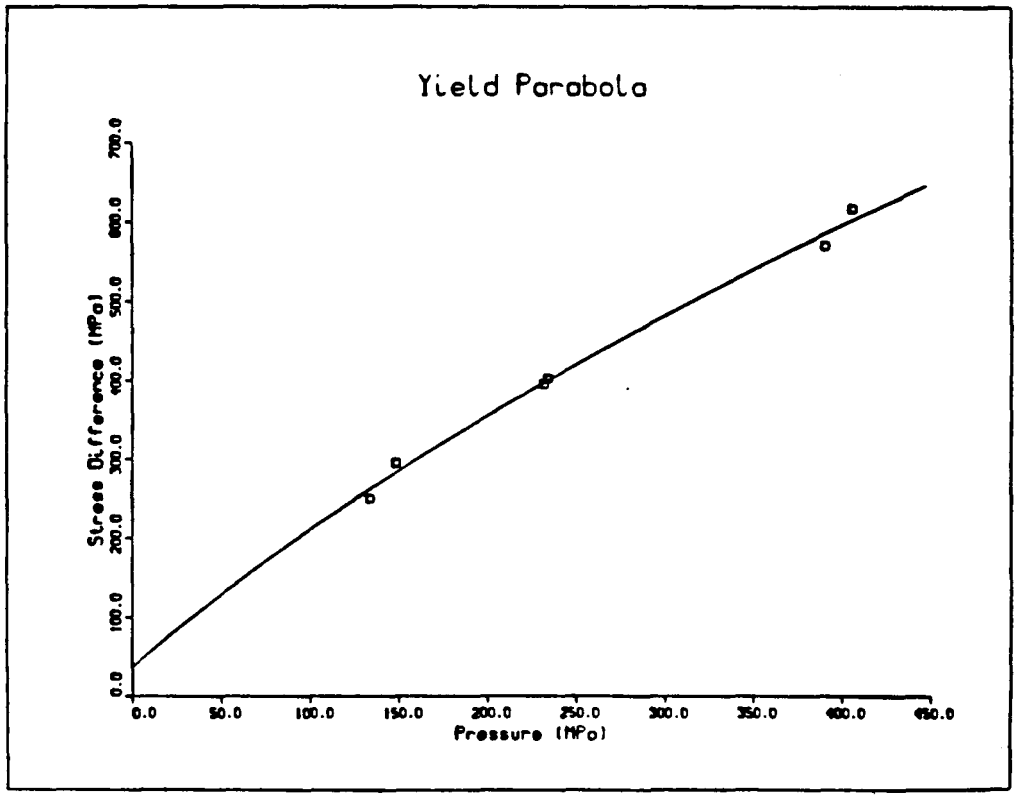

FIGURE 6 Inverse parabola yield function fit to triaxial test data for sandstone

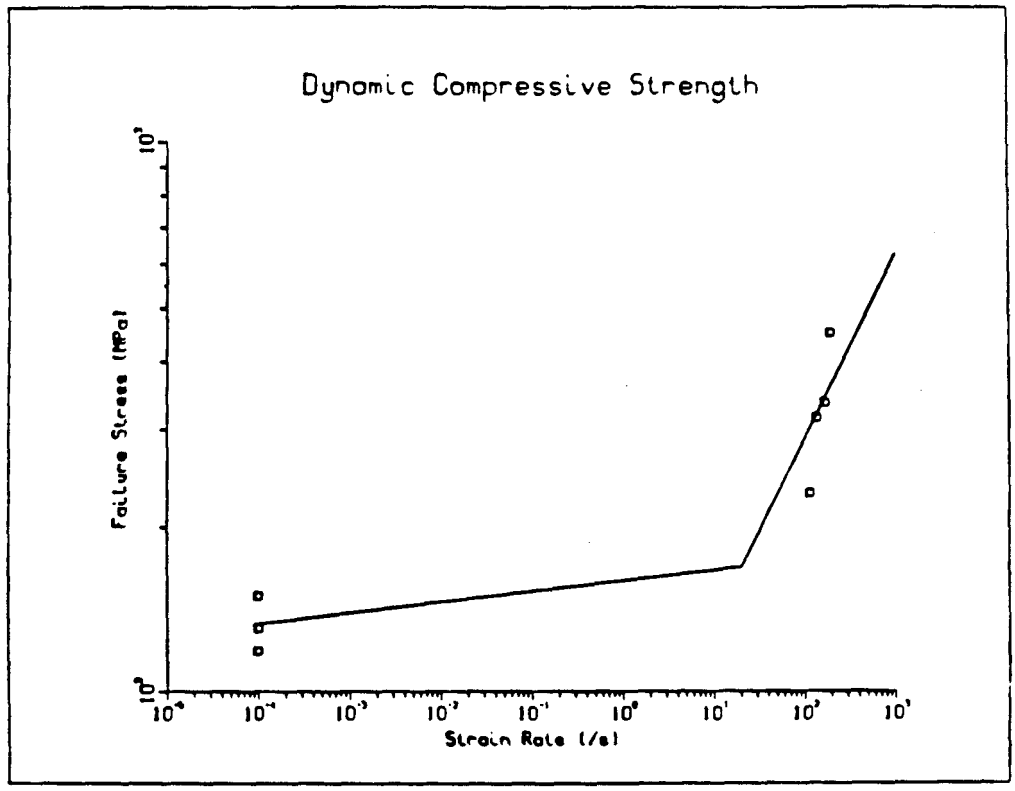

FIGURE 7 Strain rate dependence of dynamic failure stress for granite

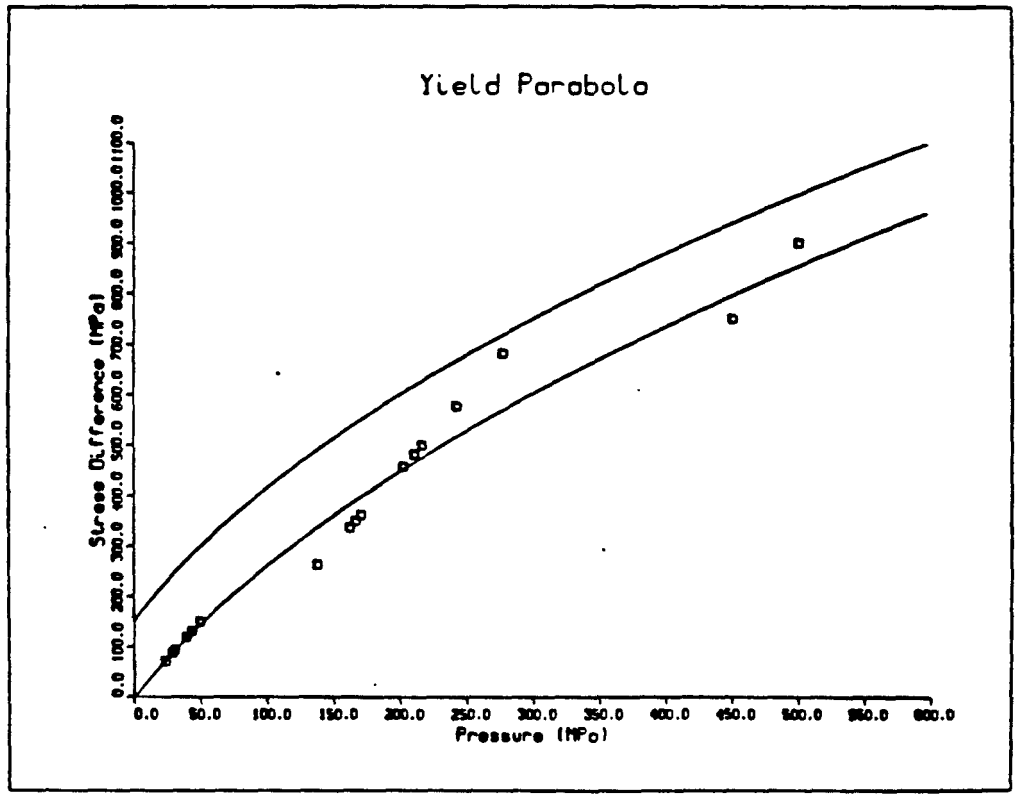

FIGURE 8 Static failure stress data for granite and inverse parabola yield function

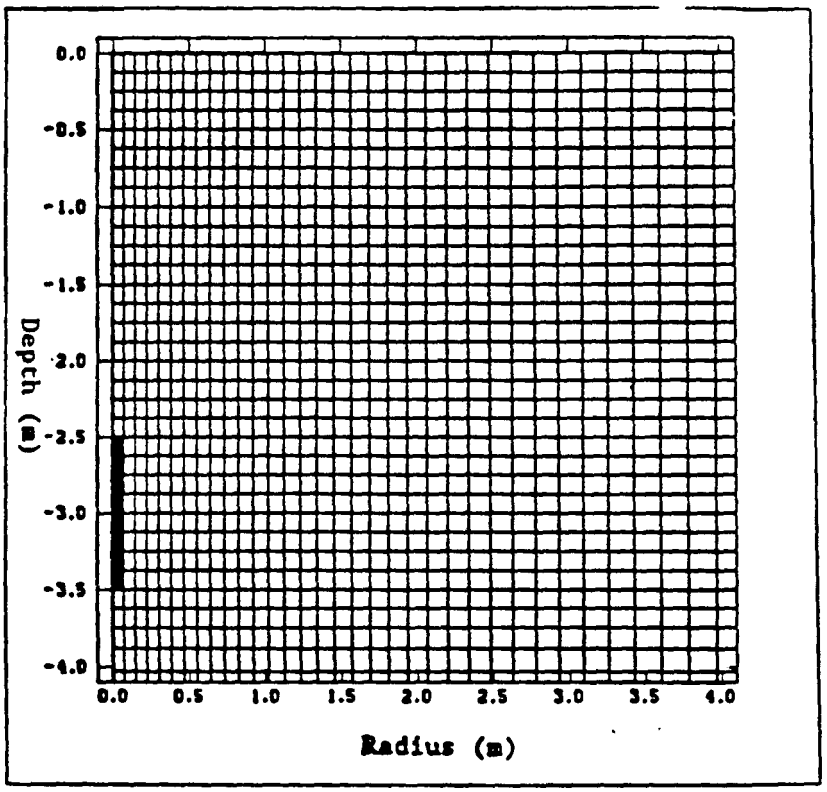

FIGURE 9 Finite element model for 3m depth-of-burial calculations

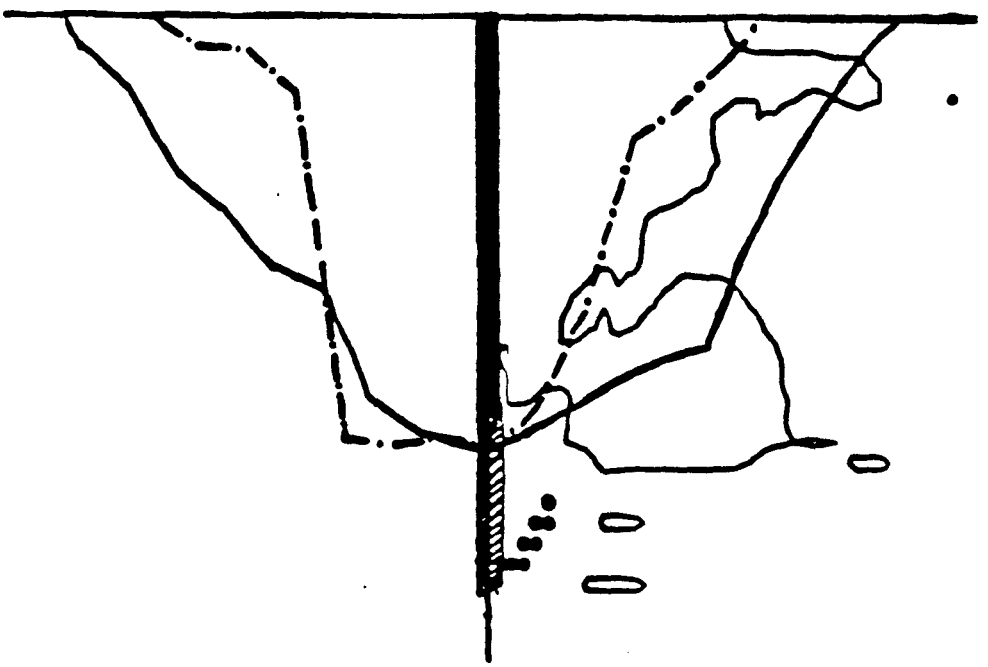

FIGURE 10 Comparison of calculated fragmented region limit with excavated crater profiles for a one-meter APEX 1220 charge centered at a depth of three meters in granite

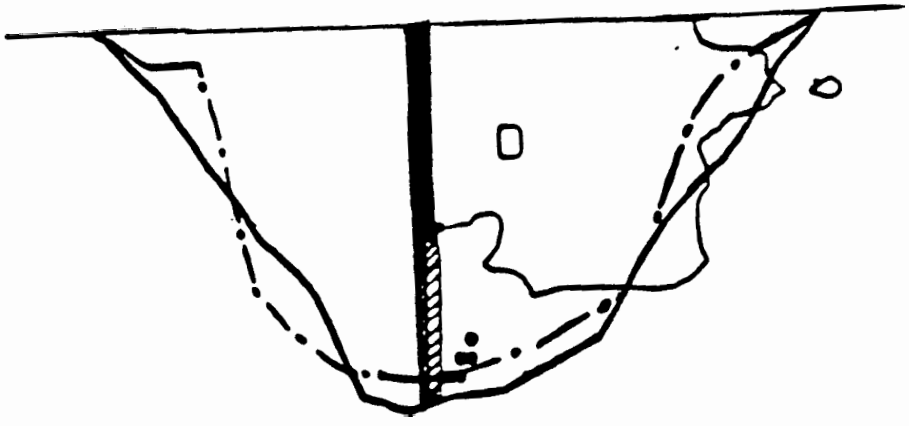

FIGURE 11 Comparison of calculated fragmented region limit with excavated crater profile for a one-meter APEX 1220 charge centered at a depth of two meters in granite

FIGURE 12 Comparison of calculated fragmented region limit with an excavated crater profile for a one-meter APEX 1220 charge centered at a depth of four meters in granite

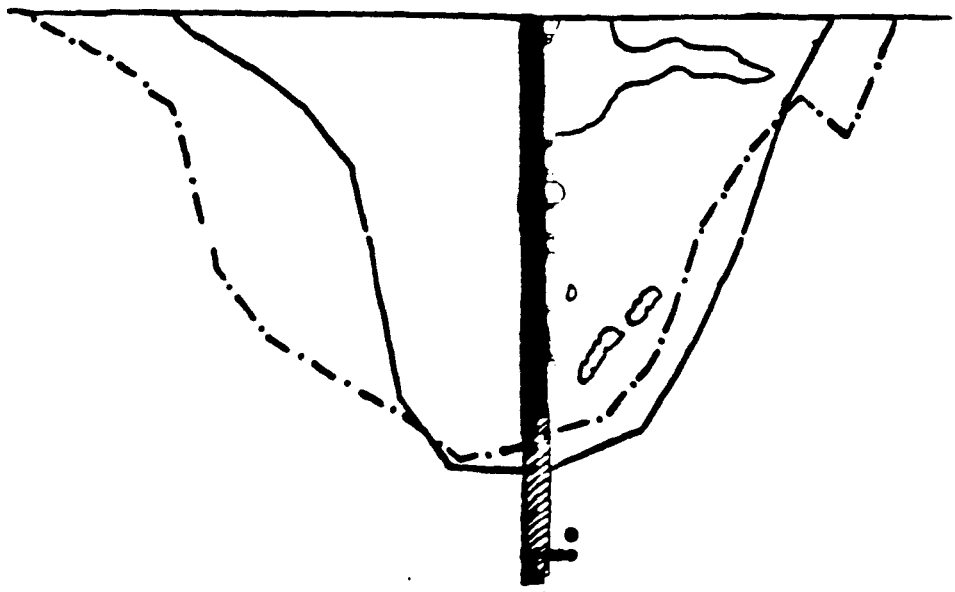

FIGURE 13 Comparison of calculated fragmented region limit with excavated crater profiles for a one-meter ANFO charge centered at a depth of three meters in granite at a basalt dike

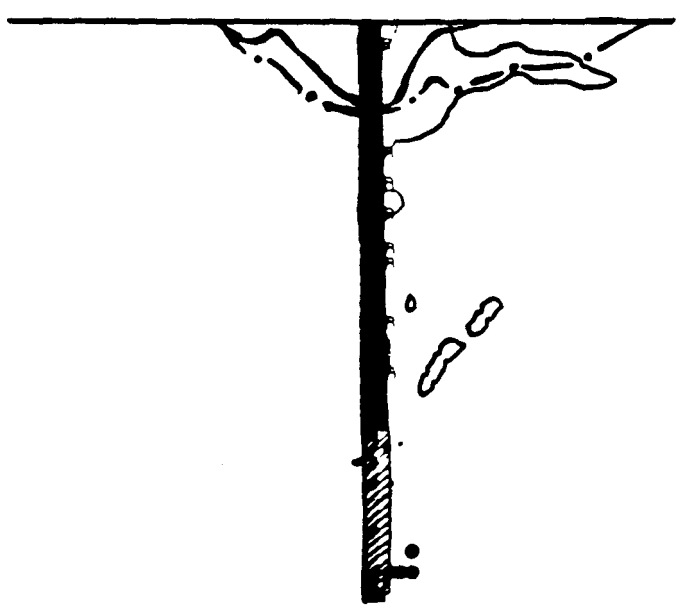

FIGURE 14 Comparison of calculated fragmented region limit with an excavated crater profile for a one-meter ANFO charge with low detonation velocity centered at a depth of three meters in granite

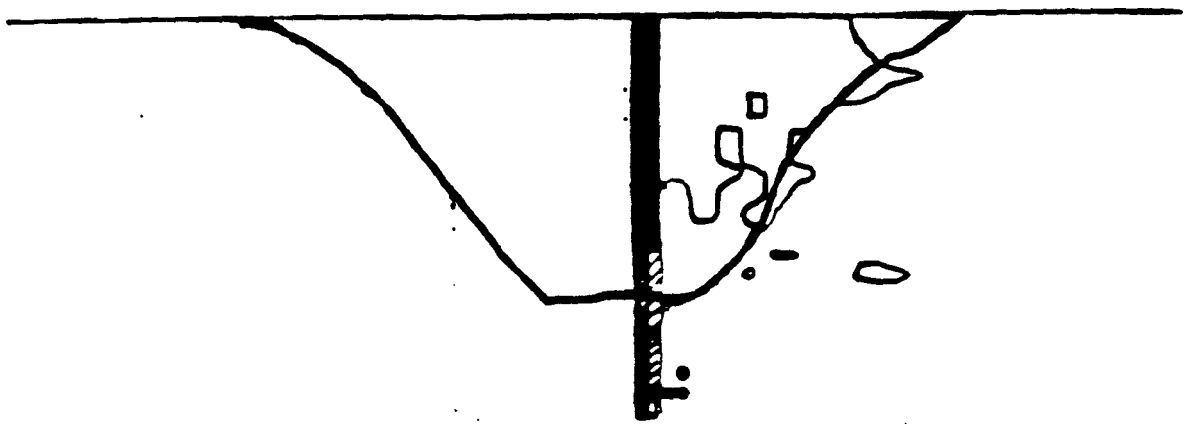

FIGURE 15 Comparison of calculated fragmented region limit with an excavated crater profile for a one-meter ANFO charge centered at a depth of two meters in granite

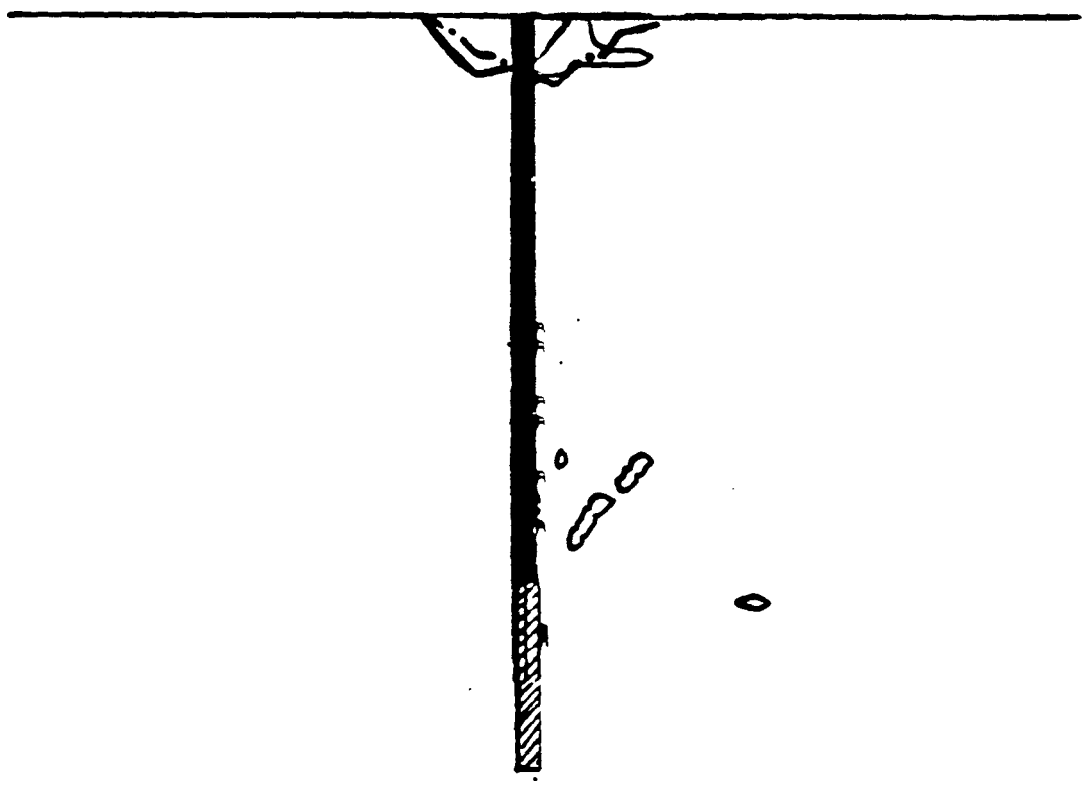

FIGURE 16 Comparison of calculated fragmented region limit with excavated crater profiles for a one-meter ANFO charge centered at a depth of four meters in granite